Video-Based, In-situ Microrheological Analysis of Hydrogel Synthesis

ChuTe Chen, Rebekah Finster, Kristofer Reyes

C. Chen, R. Finster, K. Reyes (kreyes3@buffalo.edu)
Department of Materials Design and Innovation
120 Bonner Hall, University at Buffalo
North Campus, Buffalo, NY 14260, USA

Abstract

Hydrogels composed of silk fibroin and various crosslinking agents hold significant promise for biomedical applications due to their tunable mechanical properties and biocompatibility. However, optimizing their gelation characteristics remains a complex challenge. In this study, we integrate Multiple Particle Tracking (MPT) and Differential Dynamic Microscopy (DDM) to quantitatively characterize the gelation process of silk-based hydrogels. Using polystyrene tracking beads and time-resolved microscopy, we monitored transitions from fluid-like to elastic states. MPT analysis facilitated detailed trajectory reconstruction and calculation of rheological parameters such as mean-square-displacement, viscosity, and moduli, yielding a gelation time of 22–33 seconds. In parallel, DDM enabled automated, parameter-free extraction of comparable rheological properties, with gelation times of 30–37 seconds. Both techniques captured the critical crossover point where storage modulus surpasses loss modulus, corroborating the onset of gelation. While MPT required careful parameter optimization and user oversight, DDM offered streamlined data analysis. The resulting insights, together with machine learning-driven optimization approaches, pave the way for more efficient hydrogel formulation design.

1. Introduction

Hydrogels are highly water-retentive polymeric networks that maintain structural integrity while exhibiting significant flexibility and porosity. These materials have gained prominence in biomedical fields due to their biocompatibility, tunable mechanical properties, and resemblance to natural tissues. Applications span a wide range, including tissue engineering, drug delivery, wound dressings, and bioprinting. Designing hydrogels with tailored properties often involves complex parameter spaces, including polymer concentrations, crosslinker types, porosities, and functional additives. Historically, material optimization has relied on trial-and-error methods, which are costly and time-consuming. The integration of artificial intelligence (AI) and machine learning (ML) methods into hydrogel research is transforming this landscape by accelerating material discovery, reducing experimental burden, and enabling more precise optimization of properties.

A variety of AI and ML techniques have been applied to hydrogel design and characterization. Bayesian optimization, for instance, focuses experimental efforts on the most promising formulations. Hashemi et al. employed this approach to develop a biomaterial ink composed of chitosan, gelatin, and agarose[1]. By iteratively refining the search space, Bayesian optimization efficiently navigated complex parameter sets, focusing on hydrogel candidates with desirable rheological and biological properties. Similarly, Ege et al. analyzed heterogeneous datasets using extreme gradient boosting (XGB) to identify how parameters like gelatin and crosslinker concentrations influenced scaffold stiffness [2]. Their results demonstrated that increasing gelatin content could weaken the scaffold, while smaller pore sizes increased gel stiffness—insights that would have been more difficult to extract using conventional statistical methods.

Deep learning (DL) techniques, including deep neural networks (DNNs) and convolutional neural networks (CNNs), have also proven valuable. Allencherry et al. utilized a DNN to predict bioprinting quality of alginate-based hydrogels crosslinked with calcium chloride [3]. By learning nonlinear relationships between composition and printability, the DNN enabled rapid optimization of printing parameters, enhancing consistency and reducing experimental trials. In peptide-based hydrogel design, Li et al. demonstrated that ML algorithms such as XGB could outperform traditional approaches like random forests and linear regression in predicting gel-forming ability and properties [4]. Xu et al. further extended ML capabilities by using a support vector machine (SVM) model to classify peptide sequences into gel-forming and non-gel-forming groups, expanding the design space beyond previously known sequences and enabling the generation of thousands of new candidates [5].

Beyond the identification of promising hydrogel compositions, AI-driven models can predict mechanical and thermal properties. Molecular dynamics (MD) simulations, combined with artificial neural networks (ANNs), have been used to model how changes in polymer volume fractions affect thermal conductivity, Young's modulus, and overall strength [6] [7]. Similarly, response surface methodology (RSM) and ANN-based models have guided the formulation of hydrogel dressings composed of polyvinyl alcohol (PVA), chitosan, and starch [8]. By systematically varying component ratios and integrating data-driven insights, optimal compositions were determined based on criteria such as swelling ratio, gel content, and water vapor transmission rate. The addition of zinc oxide nanoparticles and heparin further enhanced

mechanical strength, antibacterial effects, and cytocompatibility, a process facilitated by AI-driven optimization.

Advanced AI approaches also integrate finite element analysis (FEA) and imaging data to model hydrogel microstructures and mechanical responses [9]. For example, a CNN-based regression model trained on FEA simulations and microstructural images of bioglass-collagen hydrogels effectively predicted Young's modulus and Poisson's ratio. Such models can handle the nonlinearities that arise during large deformations, providing accurate predictions without excessive computational cost.

Deep learning frameworks have been employed to map polymer network structures to macroscale mechanical properties. Starting from mesoscopic scale models, researchers have used DNNs and 3D CNNs to predict stress-stretch curves under uniaxial tension, showing remarkable accuracy and versatility [10]. These end-to-end approaches are valuable for designing gels with precise mechanical characteristics, essential for applications like load-bearing tissue scaffolds.

Silk, derived from the cocoons of the silkworm, is a fibrous protein known for its robust mechanical strength, biocompatibility, and tunable degradation properties. These attributes make silk fibroin an attractive candidate for developing hydrogels suited to a wide range of biomedical applications[11]. Silk hydrogels can be tailored in terms of stiffness, porosity, and degradation rate through alterations in silk concentration, crosslinking, and processing conditions. Such tunability makes them valuable as scaffolds for tissue engineering, carriers for controlled drug release, and matrices for 3D cell culture [12].

Multiphysics modeling, combined with AI, was utilized to optimize drug release kinetics from a silk fibroin-based hydrogel for controlled delivery of vincristine [13]. The integration of computational simulations, inverse analysis, and continuum mechanics predicted gel deformation, degradation, and drug diffusion, revealing that gel deswelling over time accelerated drug release. The strong agreement between simulation and experimental data highlights the power of combined ML and computational physics approaches in refining drug delivery strategies.

Forming accurate models requires gathering large amounts of experimental data, which is time intensive and costly. In order to automate the data collection for the gelation time of a silk-based hydrogel, Differential Dynamic Microscopy (DDM) is employed. DDM is performed on a video of a silk gel containing tracking particles undergoing gelation. The results of the DDM process are compared to the results of a traditional method; Multiple Particle Tracking (MPT). The results of these methods can then be employed to optimize the gelation time of the hydrogel by exploring various gel formulations using a Bayesian learning model. The resulting Bayesian model will have the ability to facilitate optimal decision- making under uncertainty, enable precise control of the gelation process and enhance performance across different applications [14].

2. Methods

2.1 Video Data

Samples of volume 100 to 400μL were imaged in open 8-well microscopy dishes using an OpenTrons Liquid Handling Robot. Samples contained various ratios of silk, horseradish peroxidase (HRP), and hydrogen peroxide, along with carboxylate-functionalized polystyrene tracking beads. The beads were 100nm in diameter and included at a density of about 100 beads per 40X40μm^2 of field. The samples were held at 30°C, and images were taken 100μm above the slide at an acquisition rate of 100Hz. Videos of 1000 frames were captured as the samples gelled.

2.2 MPT

Multiple particle tracking (MPT) was performed following the procedures outlined in the Trackpy tutorial (http://soft-matter.github.io/trackpy/v0.6.4/tutorial/walkthrough.html). Briefly, two-dimensional time-lapse image sequences were obtained with a known time interval Δt between frames. After loading each frame into a Python environment, particles were identified using *trackpy.locate*, which employs bandpass filtering and intensity-based thresholding to detect bright spots corresponding to particle centers. Features were refined to sub-pixel accuracy by fitting a two-dimensional Gaussian, ensuring precise estimates of particle coordinates (x,y).

Trajectory construction was achieved by linking particle positions across consecutive frames with *trackpy.link*. Internally, this linking process minimizes the total cost of assignments between particle sets in successive frames, typically based on Euclidean distance,

$$d_{ij} = \sqrt{\left(x_i^{t+1} - x_j^t\right)^2 + \left(y_i^{t+1} - y_j^t\right)^2} \tag{1}$$

Where d_{ij} is the distance between a particle *j* in frame t and a particle *i* in frame t+1. A maximum allowed displacement was specified to prevent linking of physically implausible jumps, and brief track interruptions were addressed by allowing limited "memory" for gap closure.

With continuous particle trajectories established, mean-square-displacement (MSD) calculations were performed using *trackpy.imsd.* The MSD as a function of lag time,

$$\tau = n\Delta t$$

Where n is an integer number of frames, was computed as,

$$MSD(\tau) = \langle [x(t + \tau) - x(t)]^2 + [y(t + \tau) - y(t)]^2 \rangle \tag{2}$$

Where the angle brackets denote an ensemble average over all particles and all starting times t. This MSD analysis enables characterization of particle transport properties and comparison with theoretical models of diffusion or directed motion.

The complex modulus can be extracted from the MSD using the Generalized Stokes-Einstein Relation (GSER). First, the time dependent MSD, $\langle \Delta r^2(t) \rangle$, obtained from the particle trajectories, is converted into a frequency-domain quantity via a Fourier transform. The MSD is related to the linear viscoelastic compliance $J(\omega)$ and ultimately to the complex modulus $G^*(\omega)$ by the GSER. For spherical tracer particles of radius, a at thermal equilibrium and temperature T, the relation can be written as:

$$G^*(\omega) = \frac{k_b T}{\pi a i \omega \langle \Delta \tilde{r}^2(\omega) \rangle} \tag{3}$$

Where k_b is Boltzmann's constant, and $\langle \Delta \tilde{r}^2(\omega) \rangle$ is the Fourier transform of the MSD. In practice, one often first computes $J(\omega)$ from the MSD (using established integral transform methods) and then inverts it to find,

$$G^*(\omega) = \frac{1}{J(\omega)} \tag{4}$$

The storage modulus, $G'(\omega)$, representing the elastic component, and the loss modulus, $G''(\omega)$, representing the viscous component, are then obtained by taking the real and imaginary parts of $G^*(\omega)$. To determine gelation time from these viscoelastic parameters, the sample's evolving mechanical properties are monitored over time as the system transitions from a liquid-like to a solid-like state. In many cases, the gel point can be recognized when $G'(\omega)$ and $G''(\omega)$ intersect at a particular frequency. The viscosity can be extracted under the assumption that the material behaves as a Kelvin-Voigt fluid at low frequencies, where the loss modulus scales linearly with omega. In this regime we have,

$$G''(\omega) = \eta \omega \tag{5}$$

To determine η, a linear fit is applied to the data points of $G''(\omega)$ versus ω using a least-square regression. After curve fitting, the optimized parameter provides the best-fit viscosity value.

The elasticity (E) is taken as the average storage modulus across the frequency range of interest:

$$E = \langle G'(\omega) \rangle \tag{6}$$

By averaging the storage modulus over multiple frequencies, we mitigate the impact of measurement noise at any single frequency. The resulting E value reflects the characteristic elastic resistance of the material to deformation under small-strain oscillations.

2.3 DDM

Differential dynamic microscopy (DDM) was employed to quantify particle dynamics by analyzing the temporal fluctuations in a series of digital images. First, a time-lapse sequence of two-dimensional intensity fields, $I(r,t)$ was collected with a known sampling time Δt. Each image was Fourier-transformed to obtain $\bar{I}(q,t)$ where q is the spatial frequency (wavevector) and r is the real-space coordinate. The core quantity of DDM, the image structure function, $D(q,t)$, was then computed as the ensemble average of the squared difference between images separated by time lag t:

$$D(q,t) = \langle |I(q,\ t_0 + t) - I(q,\ t_0)|^2 \rangle_{t_0} \tag{7}$$

Where $I(q,t)$ is the Fourier transform of image $I(x,t)$ [15].

Once the image structure function is found, the MSD can be quantified by:

$$\langle \Delta r^2(t) \rangle = \frac{-4}{q^2} \ln\left(1 - \frac{D(q,t) - B(q)}{A(q)}\right) \tag{8}$$

Where A(q) is the spatial intensity correlation and B(q) is the noise of the detection chain [15][16].

From here, all other quantities of interest are calculated similarly to the MPT method.

3. Results and Discussion

3.1 Observations from the raw data video

The time-resolved microscopy images reveal distinct phases in the evolution of particle behavior during soft material synthesis and gelation over a 49-second period. In **Figure 1**, At the initial state (t=0s), a single particle is clearly visible at position A. During the synthesis phase (t=1-33s), the particle demonstrates random motion as it traverses through positions B and C, indicating the material's fluid-like behavior. A critical transition occurs at t=33s when the particle settles at position D, marking the onset of gelation and the material's transformation from a viscous to an elastic state. In the final phase (t=33-49s), while maintaining its position at D, the particle exhibits a distinctive pulsing behavior characterized by periodic fluctuations in its apparent size, as evidenced by the radial arrows in the last two frames. This pulsing phenomenon, captured at 20 frames per second with image dimensions of 920×918 pixels, provides visual confirmation of the material's transition from a mobile to a gelated state.
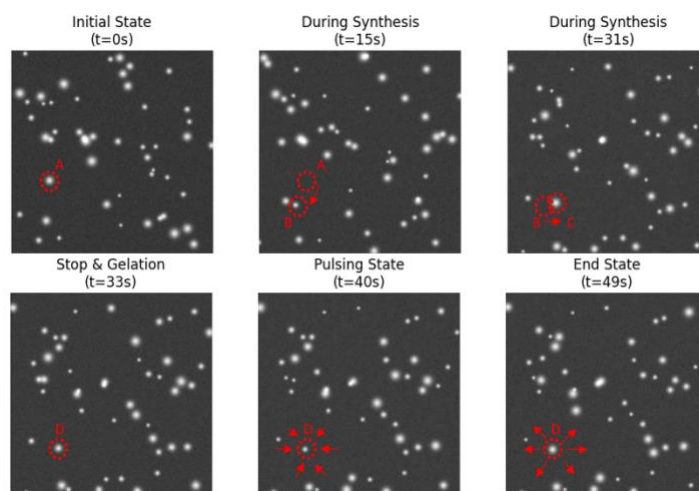

Figure 1. Time-resolved microscopy images showing the evolution of a particle during soft material synthesis and gelation. The sequence captures key stages over 49 seconds.

3.2 Multiple Particle Tracking (MPT) Analysis

MPT analysis was performed on silk hydrogel samples to estimate gel times and characterize the gelation process. The results revealed several key findings:
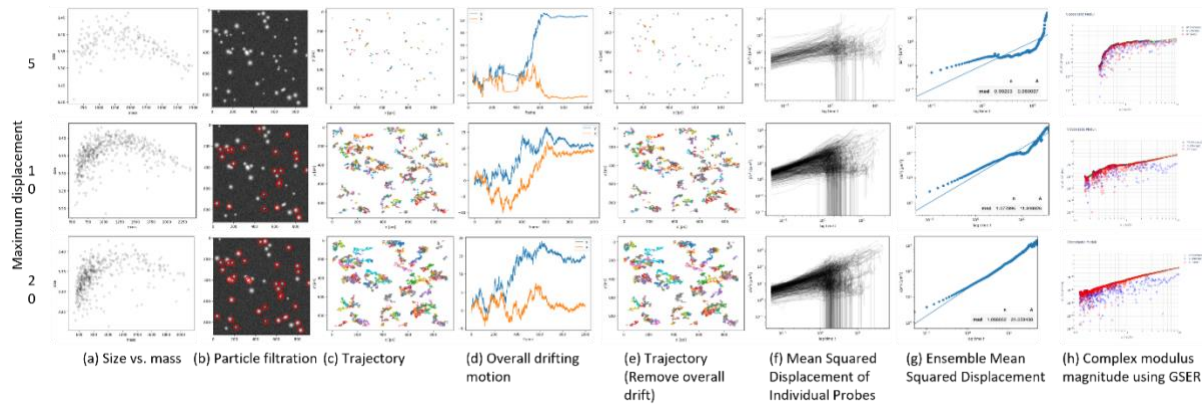
Particle Detection Optimization: **Figure 2** demonstrates the optimization of particle detection using different diameter and minmass parameters. The optimal combination (diameter=11, minmass=400) achieved balanced particle detection by effectively identifying true particles while filtering noise. Larger diameters(19) tend to merge nearby particles, while smaller diameters (7) miss particles, especially at high minmass. Lower minmass values (200) introduce false positives from noise, while higher values (800) are too restrictive and miss legitimate particles. The trends indicate that increasing either parameter enhances selectivity - higher minmass reduces detection of dim features, while larger diameters reduce

detection of small features. The intermediate parameter values provide the best compromise between detection sensitivity and noise rejection.
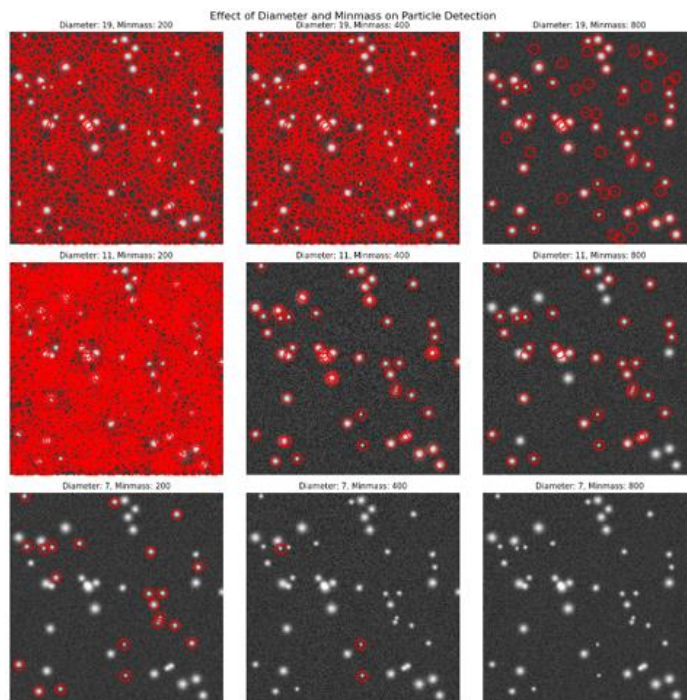
Figure 2. The 3x3 figure demonstrates particle detection optimization using different diameters (19, 11, 7 pixels) and minmass (200, 400, 800) parameters. The optimal combination (diameter=11, minmass=400) in the center image achieves balanced particle detection by effectively identifying true particles while filtering noise.

Trajectory Analysis: The comprehensive workflow of Multiple Particle Tracking (MPT) analysis, illustrated in **Figure 3**, demonstrates the effects of varying maximum displacement parameters on particle trajectory analysis. Initial particle detection utilized size-mass correlation analysis, followed by refined particle selection based on multiple criteria including size, mass, and eccentricity to eliminate spurious features. Trajectory analysis progressed from raw trajectories to drift correction, with larger maximum displacement values enabling tracking of faster-moving particles at the cost of potentially misidentified trajectories. Individual probe Mean Squared Displacement (MSD) calculations revealed variations in particle mobility, while ensemble-averaged MSD provided insights into collective particle behavior. The analysis culminated in the conversion to complex modulus using the Generalized Stokes-Einstein Relation (GSER). Notably, the maximum displacement parameter critically influenced trajectory linking accuracy, with smaller values offering more reliable tracking but potentially missing fast-moving particles, and larger values capturing more dynamic motion but risking incorrect particle linking, particularly in concentrated samples or during rapid gelation phases.

(a) Size vs. mass (b) Particle filtration (c) Trajectory (d) Overall drifting motion (e) Trajectory (Remove overall drift) (f) Mean Squared Displacement of Individual Probes (g) Ensemble Mean Squared Displacement (h) Complex modulus magnitude using GSER

Figure 3. Illustration of the comprehensive workflow of Multiple Particle Tracking (MPT) analysis, demonstrating the effects of different maximum displacement parameters on particle trajectory analysis in silk hydrogels.

Rheological Parameters: Table 1 presents the particle properties and rheological parameters obtained through MPT. The G*, G', and G'' versus annular frequency plot (**Figure 4**) shows that G' exceeds G'' near the 0.19 ~ 0.23 (rad/s) region, suggesting a transition from predominantly viscous to predominantly elastic behavior. After conversion, the gel time was extracted as 22 ~ 33 seconds.

	crossover_times (t)	omega (rad/s)	msd	G_star	G_prime	G_double_prime
0	2.60	2.42	1.704341	5.208686e-15	2.345060e-15	4.650925e-15
1	2.65	2.37	2.773879	3.200348e-15	1.234134e-15	2.952820e-15
2	2.70	2.33	3.797197	2.337877e-15	8.326734e-16	2.184565e-15
3	2.75	2.28	4.730196	1.876747e-15	6.252602e-16	1.769528e-15
4	3.05	2.06	5.653828	1.570154e-15	4.758236e-16	1.496321e-15
...	...	...	...	...	...	...
284	38.75	0.16	115.246402	7.702956e-17	-2.397282e-17	7.320421e-17
285	38.85	0.16	115.639113	7.676796e-17	-1.526354e-17	7.523526e-17
286	38.95	0.16	116.158168	7.642493e-17	-4.544683e-17	6.144391e-17
287	39.05	0.16	116.776895	7.602000e-17	-6.825225e-17	3.347641e-17
288	39.15	0.16	120.844302	7.346130e-17	-6.087790e-17	4.111501e-17

289 rows × 6 columns

**Table 1.** Particle properties and rheological parameters obtained through Multiple Particle Tracking (MPT).
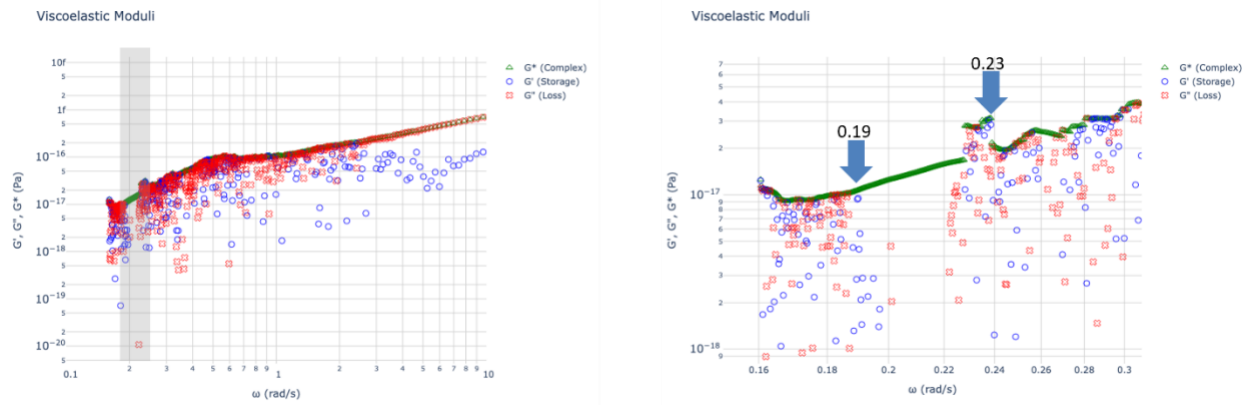
Figure 4. The G*, G', and G'' versus the annular frequency plot. The G' exceeds the G'' near 0.19 ~ 0.23 (rad/s) region which suggests a transition from predominantly viscous to predominantly elastic behavior. After conversion, the gel time can be extracted as 22 ~ 33 sec.

### 3.3 Differential Dynamic Microscopy (DDM) Analysis

DDM analysis was conducted on the same silk hydrogel samples to compare with MPT results and evaluate its effectiveness in characterizing gelation kinetics. The key findings include:

Image Structure Function Analysis: Figure 5 illustrates the systematic approach for extracting Mean Square Displacement (MSD) from image structure function analysis. The experimental image structure function D(q,t), signal amplitude A(q), and noise baseline B(q) were visualized and analyzed to calculate MSD curves for various wave vectors.
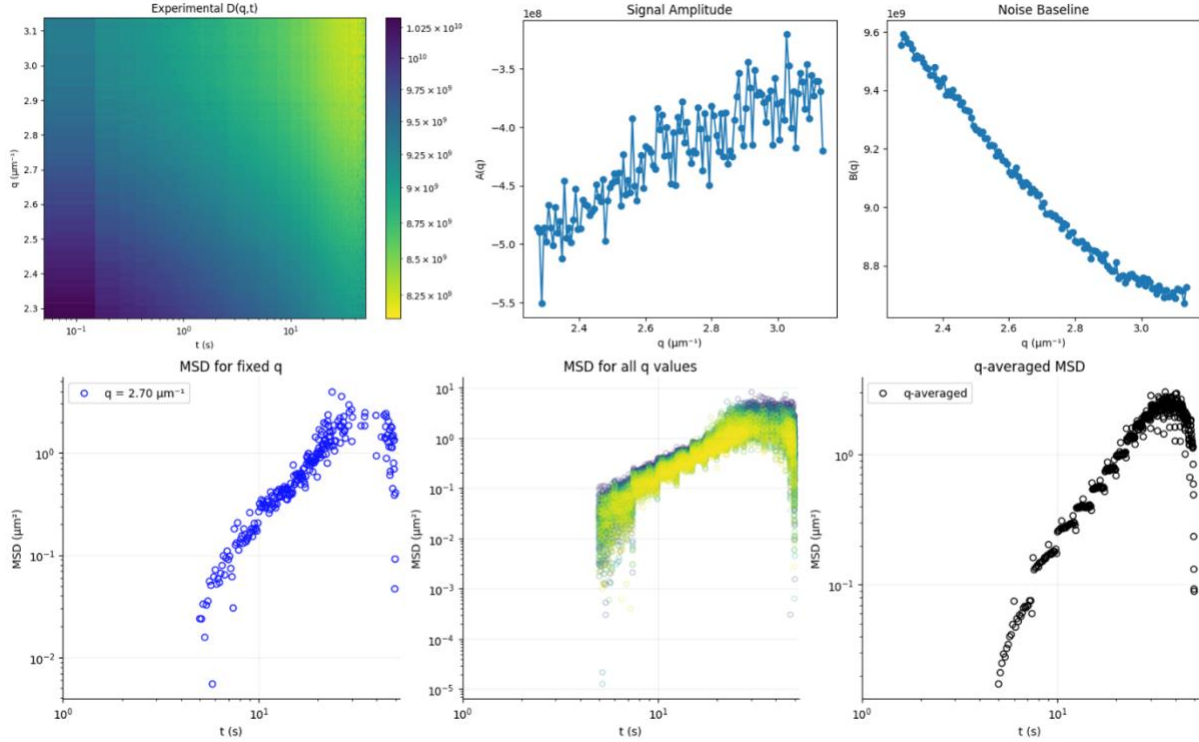
Figure 5. The systematic approach for extracting Mean Square Displacement (MSD) from image structure function analysis. The top row presents: (a) the experimental image structure function D(q,t) visualized as a color map, (b) the signal amplitude A(q) showing fluctuations across wave vectors, and (c) the noise baseline B(q) exhibiting a decreasing trend with increasing q. The bottom row illustrates the MSD analysis sequence: (d) MSD calculated for a fixed wave vector q = 2.70 μm⁻¹, (e) MSD curves obtained for all analyzed q values displayed as an overlay of multiple traces, and (f) the final q-averaged MSD result. The mathematical relationship between these parameters is governed by Equation (8), which enables the conversion of structure function measurements into MSD values. This comprehensive analysis provides a robust method for characterizing particle dynamics across multiple spatial frequencies.

MSD Evolution: Figure 6 demonstrates the changes in MSD over time during particle synthesis and gelation, revealing three distinct phases. The R1 phase showed steadily rising MSD, indicating active particle movement. The R2 phase (30-41 seconds) exhibited peak MSD, coinciding with the beginning of gelation. In the R3 phase, the MSD decreased, reflecting reduced particle mobility.
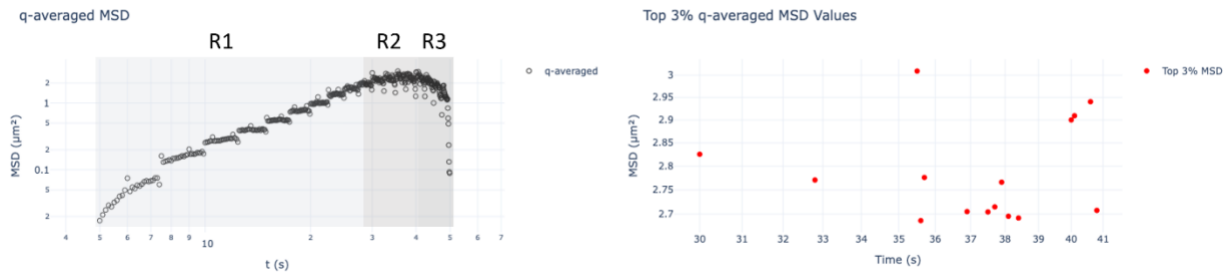
Figure 6. Illustration of the changes in Mean Square Displacement (MSD) over time during particle synthesis and gelation, revealing three distinct phases. (a) In the R1 phase, the MSD steadily rises, indicating the particle's active movement during the early stages of synthesis. This corresponds to the particle's motion from positions A to C seen in the microscopy images of Figure 1. The MSD reaches its peak in the R2 phase (30-41 seconds) as shown in (b), coinciding with the particle stopping at position D, marking the beginning of gelation as observed in Figure 1. Finally, in the R3 phase, the MSD decreases, reflecting the particle's reduced mobility and pulsing behavior at its final position. This pattern in the MSD graph effectively captures the transition from the particle's initial free movement to its eventual fixed state in the gel, providing a clear picture of the particle's behavior throughout the synthesis process.

Rheological Parameters: Table 2 presents the particle properties and rheological parameters obtained through DDM. The G*, G', and G'' versus annular frequency plot (**Figure 7**) shows that G' exceeds G'' near the 0.17 ~ 0.21 (rad/s) region, suggesting a transition from predominantly viscous to predominantly elastic behavior. After conversion, the gel time was extracted as 30 ~ 37 seconds.

	crossover_times (t)	omega (rad/s)	msd_avg_ddm	G_star	G_prime	G_double_prime
0	5.3	1.19	-0.537211	-1.652494e-14	NaN	NaN
1	5.4	1.16	-0.437532	-2.028969e-14	NaN	NaN
2	6.1	1.03	-0.406496	-2.183877e-14	NaN	NaN
3	6.2	1.01	-0.383393	-2.315477e-14	NaN	NaN
4	6.4	0.98	-0.363759	-2.440458e-14	NaN	NaN
...	...	...	...	...	...	...
208	49.0	0.13	1.003438	8.846965e-15	7.613246e-16	8.814147e-15
209	49.3	0.13	1.230623	7.213726e-15	2.509254e-15	6.763245e-15
210	49.4	0.13	1.012782	8.765339e-15	7.970887e-15	3.646385e-15
211	49.8	0.13	0.982009	9.040017e-15	7.989123e-15	4.230345e-15
212	49.9	0.13	1.015440	8.742393e-15	9.746943e-16	-8.687888e-15

213 rows × 6 columns

Table 2. Particle properties and rheological parameters obtained through Differential Dynamic Microscopy (DDM).
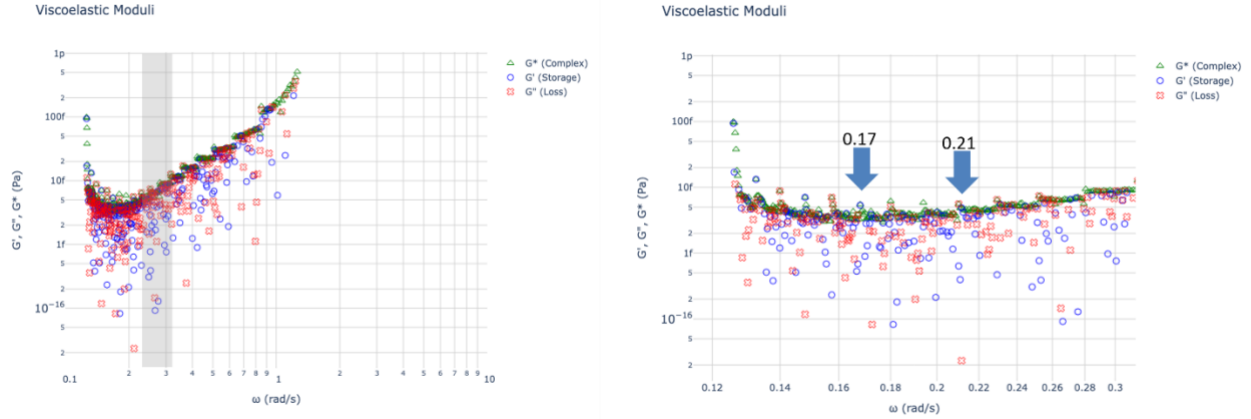
Figure 7. The G*, G', and G'' versus the annular frequency plot. The G' exceeds the G'' near 0.17~ 0.21 (rad/s) region which suggests a transition from predominantly viscous to predominantly elastic behavior. After conversion, the gel time can be extracted as 30 ~ 37 sec.

3.4 Comparison of MPT and DDM

Multiple Particle Tracking (MPT) and Differential Dynamic Microscopy (DDM) both proved effective in characterizing the gelation process of silk-based hydrogels, offering complementary insights into the material's evolving properties. The gel times estimated by MPT (22 ~ 33 seconds) and DDM (30 ~ 37 seconds) showed reasonable agreement, with overlapping ranges enhancing confidence in the results and providing a robust characterization of gelation kinetics (**Table 3 and Figure 8**). The slight differences observed between MPT and DDM results can be attributed to their distinct analytical approaches: MPT offers direct visualization of individual particle trajectories, while DDM provides ensemble-averaged information across multiple spatial frequencies. These complementary perspectives contribute to a more comprehensive understanding of the complex gelation process. Operationally, DDM demonstrated significant advantages in automation, operating without user supervision or parameter tuning, while MPT required extensive user interaction for parameter fine-tuning, particularly during optical changes in gelation. Both techniques provided valuable insights into the hydrogel's dynamic properties, crucial for optimizing formulations for various biomedical applications. The combination of MPT and DDM analyses creates a powerful toolset for characterizing the dynamic properties of silk-based hydrogels during synthesis and gelation, offering a robust and multi-faceted approach to understanding these complex materials.

	Direct observation	MPT	DDM
MSD	-	91 ~ 94	0.3 ~ 0.6
Gel time (sec)	30 ~ 33	27 ~ 33	30 ~ 37
ω (rad/s)	-	0.19 ~ 0.23	0.17 ~ 0.21
G^*	-	9.4e-17 ~ 9.7e-17	1.6e-14 ~ 3.0e-14
G'	-	5.8e-18 ~ 7.3e-17	1.2e-15 ~ 2.6e-14
G"	-	6.4e-17 ~ 9.4e-17	1.5e-14 ~ 1.6e-14

Table 3. A comprehensive comparison of particle properties and rheological parameters obtained through three different analytical methods: direct observation, Multiple Particle Tracking (MPT), and Differential Dynamic Microscopy (DDM).
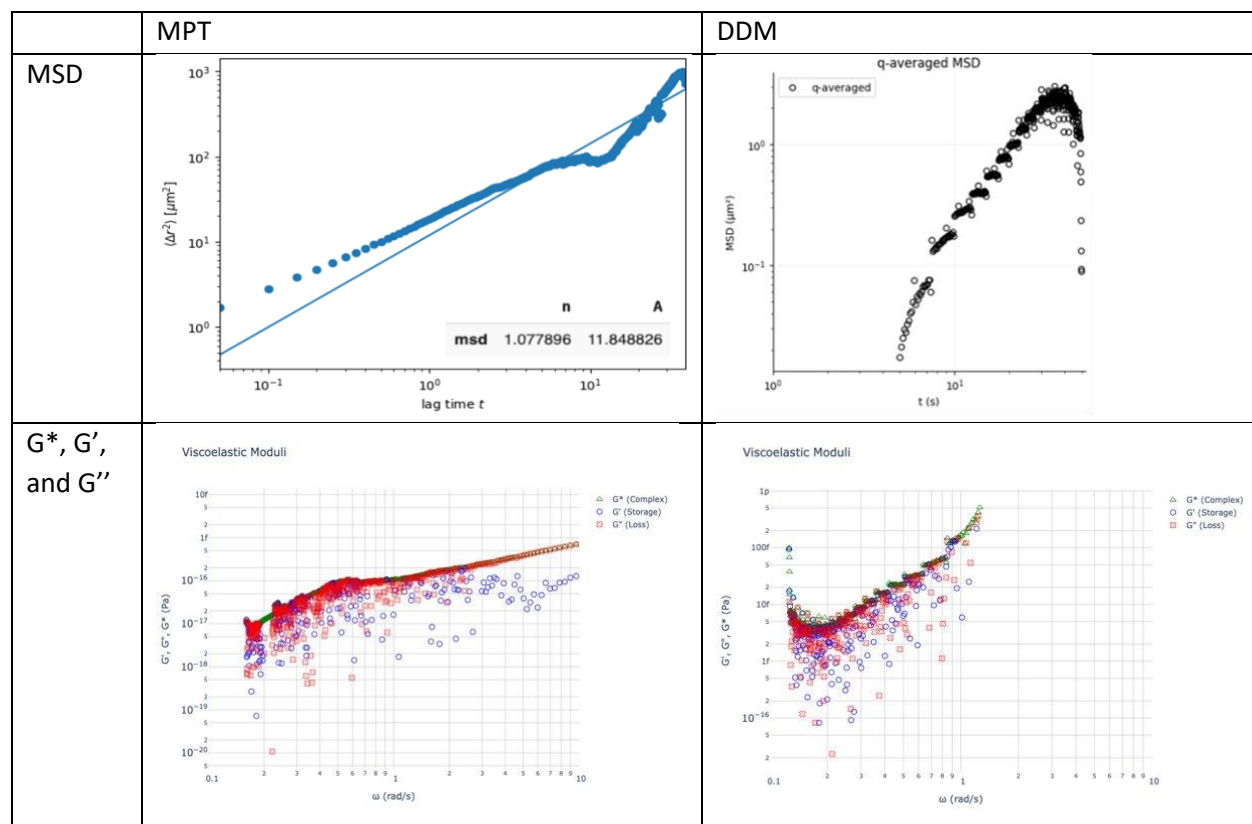
Figure 8. The comparison of particle properties and rheological parameters obtained from MPT and DDM.

4. Conclusion

This study demonstrates the effectiveness of combining Multiple Particle Tracking (MPT) and Differential Dynamic Microscopy (DDM) for characterizing the gelation process of silk-based hydrogels. Both techniques revealed three distinct phases during gelation: initial fluid-like behavior, a critical transition point, and the final gelated state. The gel times estimated by MPT (22-33 seconds) and DDM (30-37 seconds) showed reasonable agreement, enhancing confidence in the results. Both methods successfully extracted key rheological parameters, including storage modulus (G'), loss modulus (G"), and complex modulus (G*). The crossover point where G' exceeds G" provided a clear indicator of the gel point. Operationally, DDM demonstrated significant advantages in automation, operating without user supervision or parameter tuning, while MPT required more extensive user interaction, particularly during optical changes in gelation. The combination of MPT and DDM analyses creates a powerful toolset for characterizing the dynamic properties of silk-based hydrogels during synthesis and gelation, offering a robust and comprehensive understanding of these complex materials, crucial for optimizing formulations for various biomedical applications.

5. Authors Contributions

The data used in this study were provided by Dr. Kristofer Reyes from a previously conducted research study, "Engineering Gelation Kinetics in Living Silk Hydrogels by Differential Dynamic Microscopy Microrheology and Machine Learning". C. Chen led the data analysis, performing data processing, statistical evaluation, and interpretation of results. R. Finster led the literature background review, synthesizing relevant research to frame and contextualize the findings. Both authors contributed to one another's efforts by providing ideas, feedback, and critical perspectives throughout the analysis and writing process. Together, they co-wrote, reviewed, and refined the manuscript, approving the final version for submission.

6. References

[1]   A. Hashemi, M. Ezati, I. Zumberg, T. Vicar, L. Chmelikova, V. Cmiel, V. Provaznik, *Mater Today Commun* 2024, *40*, 109777.

[2]   D. Ege, A. R. Boccaccini, *Bioengineering* 2024, *11*, 415.

[3]   J. Allencherry, N. Pradeep, R. Shrivastava, L. Joy, F. Imbriacco, T. Özel, *Procedia CIRP* 2022, *110*, 360.

[4]   H. Li, X. Wang, Z. Wang, K. Y. Lam, *Macromol Biosci* 2005, *5*, 904.

[5]   T. Xu, J. Wang, S. Zhao, D. Chen, H. Zhang, Y. Fang, N. Kong, Z. Zhou, W. Li, H. Wang, *Nat Commun* 2023, *14*, 3880.

[6]   S. Shahshahani, M. Shahgholi, A. Karimipour, *J Mol Liq* 2023, *382*, 122001.

[7]   M. Islamkulov, S. Karakuş, C. Özeroğlu, *Colloid Polym Sci* 2023, *301*, 259.

[8]   A. Joorabloo, M. T. Khorasani, H. Adeli, *J Ind Eng Chem* 2021.

[9]   Y. Shokrollahi, P. Dong, P. T. Gamage, N. Patrawalla, V. Kishore, H. Mozafari, L. Gu, *Applied Sciences* 2022, *12*, 10835.

[10]   J.-A. Zhu, Y. Jia, J. Lei, Z. Liu, *Mathematics* 2021, *9*, 2804.

[11]   P. G. Chao, S. Yodmuang, X. Wang, L. Sun, D. L. Kaplan, G. Vunjak-Novakovic, *J Biomed Mater Res B Appl Biomater* 2010, *95*, 84.

[12]   A. Zheng, L. Cao, Y. Liu, J. Wu, D. Zeng, L. Hu, X. Zhang, X. Jiang, *Carbohydr Polym* 2018, *199*, 244.

[13]   Z. Gharehnazifam, R. Dolatabadi, M. Baniassadi, H. Shahsavari, A.-M. Kajbafzadeh, K. Abrinia, M. Baghani, *Int J Pharm* 2021, *609*, 121184.

[14]   R. L. Martineau, A. V Bayles, C. Hung, K. G. Reyes, M. E. Helgeson, M. K. Gupta, *Adv Biol* 2022, *6*, 2101070.

[15]   P. Edera, D. Bergamini, V. Trappe, F. Giavazzi, R. Cerbino, *Phys Rev Mater* 2017, *1*, 073804.

[16]   A. V Bayles, T. M. Squires, M. E. Helgeson, *Rheol Acta* 2017, *56*, 863.